2007 IEEE International Conference on
Robotics and Automation
Roma, Italy, 10-14 April 2007

Robust Ultrasound-Based Visual Servoing for Beating Heart Intracardiac Surgery

Marie-Aude Vitrani, Hubert Mitterhofer and
Guillaume Morel
University Pierre et Marie Curie - Paris 6
Laboratoire de Robotique de Paris
18 route du panorama,
92265 Fontenay-aux-Roses, France
{vitrani, morel}@robot.jussieu.fr

Nicolas Bonnet
University Pierre et Marie Curie - Paris 6
Pitié-Salpêtrière Hospital
Cardiac Surgery Service
47-83 boulevard de l'Hôpital
75013 Paris, France
nicolas.bonnet@psl.ap-hop-paris.fr

Abstract— **This paper presents a robust visual servoing approach for automatic guidance of an instrument. The visual sensor is an ultrasound probe that observes an instrument which is inserted into the beating heart of a patient and manipulated by a robot. The present paper provides stability analysis, robustification of the control law and an in vivo experiment.**

I. Introduction

Ultrasound imaging systems are mainly used for non operative observation of inner organs. However, they can also be employed for intervention procedures, where the surgeon moves an instrument inside a patient while observing the motion of the instrument with an outer ultrasound probe. This requires high skills for coordinating the hands holding the instrument and the probe. In fact, the ultrasound image gives only a 2D cross-section of the 3D operating region, containing no depth information. Therefore, manual ultrasound guided interventions are limited to simple tasks, such as puncture using a needle [1].

Within this context, robotic systems are being developed in order to accomplish ultrasound image-based guidance in a more performing way than manual procedures. More and more interventional systems exploit both robotics and medical imaging. They can be divided into three categories, depending on the mode of cooperation between the robot and the imaging device: via the surgeon, via 3D reconstruction or via visual servoing.

Cooperation via the surgeon: for this kind of systems, the images and the robot are two separate tools used simultaneously but independently by the surgeon; in particular, the robot never uses the information provided by the imaging system, neither directly nor indirectly. Typical examples are telemanipulated systems and some cobotic systems.

The teleoperation systems allow remote examinations. In [2], [3], [4], telemanipulators holding an ultrasound probe for the remote diagnosis are proposed. In [5], a system is proposed where the robot and the surgeon simultaneously hold an ultrasound probe. The comanipulation is used so that the surgeon can position the probe in an intuitive way. The robot's assistance allows to realize the desired displacement by guaranteeing a constant limited effort on the patient skin. In all these systems, the image is simply used to provide a view of the patient and/or instruments to the surgeon, exactly as for manual interventions. The image is never used for automatic guidance purposes.

Cooperation via 3D reconstruction: in this second class of systems, pre-or per-operative images are processed in order to reconstruct 3D information which is then used by the robot. In [6], two robots collaborate. A first robot handles the ultrasound probe. Thanks to a localization of the anatomical target in the image and geometrical model, a second robot, handling a needle, is commanded towards the computed 3D position. In vitro tests emphasize a better accuracy than with manual procedures. The system proposed by [7] allows to carry out a biopsy of the prostate. The prostate 3D model is reconstructed using the ultrasound images. Thus the robot is fed with the 3D model in order to compute the trajectory. The tests on dead bodies showed a final positioning error of about 2,5 mm. Some systems also use the images to perform, in real time, the 3D reconstruction of the desired position instead of establishing a patient model from preoperative images, [8], [9]. In these systems, the target is detected and tracked in the images. Their 3D position can then be calculated in a robot coordinate frame. The main limit of the 3D reconstruction is that geometrical errors are cumulated due to the multiple devices used for localization which results in important errors in the final robot positioning.

Cooperation via visual servoing: in this last category, the positioning error is measured directly in the image and is used to calculate the robot displacement towards the desired image position. In [10], the control is shared between the surgeon and a visual servoing loop, which is used to compensate for the physiological movements. In [11] visual servoing is used to position an ultrasound probe with respect to a phantom which geometry is known. The system is used to establish a calibration procedure for 3D ultrasound probes. Finally, a system for guiding a needle by visual servoing is proposed in [12]. It consists of an ultrasound probe and a needle manipulator with two degrees of freedom. The needle is mechanically forced to remain in the ultrasonic plane. Its orientation and its penetration are controlled automatically by a visual servoing loop. However, this research treats only

1-4244-0602-1/07/$20.00 ©2007 IEEE.

the particular case of planar tasks.

We present in this paper a system that allows for the ultrasound-based guidance of the 4 dofs of a surgical instrument inside a beating heart. First results of this research were already presented in [13], [14]. After a brief recall on these results in Sect. II, the present paper provides the most recent developments of our work: control law simplification and stability studies are provided; two controllers based on different parameterizations are compared, Sect. III; a new experimental set-up is proposed, Sect. IV. Finally, new conclusive results of in vivo experiments are presented.

II. Visually Servoed System Overview

A. System description

The overall system developed in this research is sketched in Fig. 1. It involves a robot holding an instrument, inserted into the heart through a trocar. The instrument is observed by an ultrasound probe, which images are sent in real time to a computer. In the chosen configuration, each jaw of the instrument intersects the ultrasound plane. Thus, two blobs are visible in the image, which allows for the instrument localization, thanks to appropriate image processing algorithms, see [15].

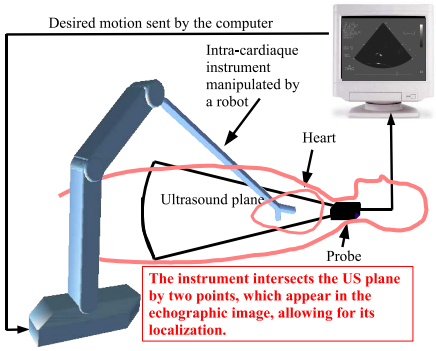

Fig. 1. System Description

More precisely, the image processing provides in real time the coordinates of the centers of gravity P_1 and P_2 of the two blobs corresponding to the instrument image. The goal of the controller is to move P_1 and P_2 at a desired location, which the surgeon specifies by simply clicking in the image. The controller is primarily based on a model mapping the instrument motion into the image space motion. It all comes down to a geometrical model which is briefly recalled in the next.

1) Geometrical modelling: In order to derive a model for the control design, a first modelling simplification consists in assuming that P_1 and P_2 coincide with the two points M_1 and M_2 that correspond to the intersection of two lines (representing the instrument jaws) and a plane Π (representing the ultrasound probe, which is assumed to provide a 2D cross-section of the 3D workspace).

Furthermore, even if the heart beats, in vivo experiments showed that the trocar center (fulcrum point), can be supposed to be fixed in the probe frame. This point is denoted by the point T. Its location with respect to the robot base frame is supposed too be known thanks to a simple initialization phase at the beginning of the operation.

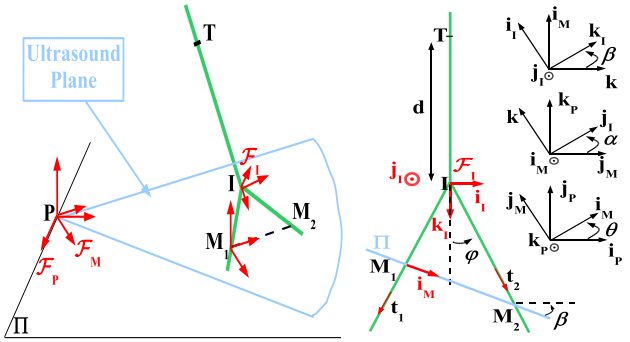

(a) Frame description (b) Parameters description

Fig. 2. System Modelling

In the next, three orthonormal coordinate frames will be used, Fig. 2(a):

- $\mathscr{F}_I = \{I; \mathbf{i}_I, \mathbf{j}_I, \mathbf{k}_I\}$ is attached to the instrument $\mathscr{I}$, with I being the intersection point between the two lines representing the jaws. The vector $\mathbf{k}_I$ is parallel to the instrument axis, Fig. 2(b).
- $\mathscr{F}_P = \{P; \mathbf{i}_P, \mathbf{j}_P, \mathbf{k}_P\}$ is attached to the ultrasound probe $\mathscr{P}$ with $\mathbf{k}_P$ perpendicular to the ultrasound plane, and P the origin of the ultrasound rays,
- $\mathscr{F}_M = \{P; \mathbf{i}_M, \mathbf{j}_M, \mathbf{k}_P\}$, where $\mathbf{i}_M$ is defined as $\mathbf{i}_M = \frac{1}{\delta}\mathbf{d}_{M_1M_2}$ with $\delta = \|\mathbf{d}_{M_1M_2}\|$[1].

Moreover, we will use in the next the following notations

$$\begin{cases} \mathbf{d}_{TI} = d\ \mathbf{k}_I \text{ and } \mathbf{d}_{IM_i} = l_i \mathbf{t}_i, \text{for } i = \{1,2\} \\ {}^I\mathbf{t}_i = [t_{ix}\ 0\ t_z]^T,\ t_{ix} = (-1)^i \sin\varphi\ ,\ t_z = \cos\varphi \end{cases}, \quad (1)$$

while the rotation from $\mathscr{F}_P$ to $\mathscr{F}_I$ will be parameterized by the ZXY Euler angles denoted θ, α and β, see Fig. 2(b).

2) Two sets of features: In order to implement robot guidance through visual servoing, a set of features describing the instrument location in the image has to be defined. In the next, we will study visual servoing for two different feature sets $\mathbf{s_1}$ and $\mathbf{s_2}$ (Fig. 3(a) and Fig. 3(b) respectively):

$$\begin{aligned} \mathbf{s}_1 &= \begin{bmatrix} {}^Px_{M_1} & {}^Px_{M_2} & {}^Py_{M_1} & {}^Py_{M_2} \end{bmatrix}^T \\ \mathbf{s}_2 &= \begin{bmatrix} {}^Px_{\bar{M}} & \delta & {}^Py_{\bar{M}} & \theta \end{bmatrix}^T \end{aligned} \quad (2)$$

where:

- $\begin{bmatrix} {}^Px_{M_i}, {}^Py_{M_i} \end{bmatrix}$ are the image coordinates of point M_i,
- $\begin{bmatrix} {}^Px_{\bar{M}}, {}^Py_{\bar{M}} \end{bmatrix}$ are the image coordinates of point $\bar{M}$ defined as the midpoint of M_1 and M_2,
- δ is the distance between M_1 and M_2,
- θ is the angle between the image axis $\mathbf{i}_P$ and $\mathbf{i}_M$.

[1]In general in this paper, we use $\mathbf{d}_{AB}$ to denote for the vector joining a point A to a point B.

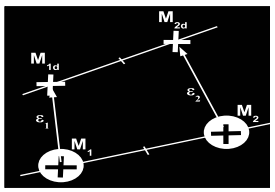

(a) Feature vector $\mathbf{s_1}$

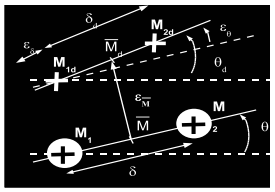

(b) Feature vector $\mathbf{s_2}$

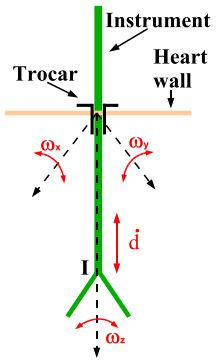

(c) Remainings dofs

Fig. 3. Features and command vectors

B. Visual servoing

1) Principle: A visual servoing loop is a controller aimed at moving a set of image features $\mathbf{s_i}$ extracted from the image toward a desired value $\mathbf{s_{id}}$. A conventional method is, for the commanded velocity $\mathbf{u}$ sent to the robot, to be calculated as:

$$\mathbf{u} = \lambda \widehat{\mathbf{J}}_{\mathbf{si}}^{-1} (\mathbf{s_{id}} - \mathbf{s_i}) = \lambda \widehat{\mathbf{J}}_{\mathbf{si}}^{-1} \varepsilon_\mathbf{i} \tag{3}$$

where λ is a positive scalar proportional gain and $\widehat{\mathbf{J}}_{\mathbf{si}}$ is the estimate of the image jacobian matrix $\mathbf{J_{si}}$ defined by:

$$\dot{\mathbf{s}}_\mathbf{i} = \mathbf{J_{si}} \mathbf{u} \tag{4}$$

2) Command vector and image jacobian matrices: As the instrument is introduced into the heart through a trocar fixed on the heart wall, only four intracardiac degrees of freedom remain, Fig. 3(c). Thus, the command sent to the robot can be expressed as:

$$\mathbf{u} = \left[\omega_y,\ \dot{d},\ \omega_x,\ \omega_z\right]^T \tag{5}$$

where $[\omega_x,\ \omega_y,\ \omega_z]^T = {}^I\Omega_{\mathscr{I}/\mathscr{P}}$ is the angular velocity of the instrument tip with respect to the ultrasound probe and $\dot{d}$ is the translation velocity of the instrument tip along $\mathbf{k_I}$. A major stage in developing a visual servoing loop is to derive the model associated to a given feature set $\mathbf{s_i}$. This was done in previous publications, namely in [13] for $\mathbf{s_1}$ and in [14] for $\mathbf{s_2}$. Both the resulting matrices can be written as:

$$\mathbf{J_{si}} = \mathbf{R_i}(\theta)\mathbf{J_i}\ ,\quad \mathbf{i} \in \{\mathbf{1},\mathbf{2}\} \tag{6}$$

where $\mathbf{R_1}(\theta)$ and $\mathbf{R_2}(\theta)$ account for the known rotation θ only, while $\mathbf{J_1}$ and $\mathbf{J_2}$, which form is recalled in the Appendix, depends on other geometrical parameters. Note that $\mathbf{J_1}$ and $\mathbf{J_2}$ are both block triangular which provides a significant increase of the control loop robustness [16].

III. Robust control from $\mathbf{s_1}$ and $\mathbf{s_2}$

While regular control schemes were developed in [13] and [14], we propose in the next a simpler implementation that avoids for any on line estimation of the probe location w.r.t. the robot. Moreover, the simplified controllers are attached with proven stability properties, which emphasizes their robustness.

A. Control law simplification

Depending on the assumptions used for the different geometrical parameters of the system, the form of the estimated inverse jacobian $\widehat{\mathbf{J}}_{\mathbf{si}}^{-1}$ will change. In particular, if the instrument is assumed to be perpendicular to the ultrasound plane, *i.e.* $\alpha = \pi$ and $\beta = 0$, then the jacobian matrices take the following simple forms:

$$\mathbf{J_{1(\pi,0)}} = \begin{bmatrix} \frac{l + d\cos\varphi}{\cos\varphi} & \frac{\sin\varphi}{\cos\varphi} & 0 & 0 \\ \frac{l + d\cos\varphi}{\cos\varphi} & -\frac{\sin\varphi}{\cos\varphi} & 0 & 0 \\ 0 & 0 & l\cos\varphi + d & l\sin\varphi \\ 0 & 0 & l\cos\varphi + d & -l\sin\varphi \end{bmatrix} \tag{7}$$

and

$$\mathbf{J_{2(\pi,0)}} = \begin{bmatrix} \frac{l + d\cos\varphi}{\cos(\varphi)} & 0 & 0 & 0 \\ 0 & -2\tan\varphi & 0 & 0 \\ 0 & 0 & d + l\cos\varphi & 0 \\ 0 & 0 & 0 & -1 \end{bmatrix} \tag{8}$$

where $l = l_1(\beta = 0) = l_2(\beta = 0) = \dfrac{\delta}{2\sin\varphi}$. Remarkably, these matrices only depend on φ, which is known from the geometrical model of the instrument, δ, that can be measured in the image and d, which can be computed from the geometrical model of the robot and from the known trocar center position. Therefore, they can be computed on line without any additional information. For this reason, they are used as the estimates for the real matrices in the control law:

$$\mathbf{u} = -\lambda \widehat{\mathbf{J}_{\mathbf{si}}^{-1}} \varepsilon_\mathbf{i} = -\lambda \mathbf{J}_{\mathbf{i}(\pi,\mathbf{0})}^{-1} \mathbf{R}_\mathbf{i}^T \varepsilon_\mathbf{i} \tag{9}$$

A very interesting feature of this control law is that it does not require any on-line estimation of the probe location with respect to the robot. This feature is quite interesting in the context of a medical application, as it allows for not using, in the system, any additional external localizer for registration. Of course, in the actual configuration, when $(\alpha,\beta) \neq (\pi,0)$ the controller does not realize a perfect kinematic decoupling for $\mathbf{s}_i$. However, as shown in the next, stability is preserved.

B. Stability Analysis

When applying control law (9), the closed loop behavior is:

$$\dot{\varepsilon}_\mathbf{i} = -\lambda\, \mathbf{J_{si}} \widehat{\mathbf{J}_{\mathbf{si}}^{-1}} \varepsilon_\mathbf{i} =: -\lambda \mathbf{A}(\mathbf{s_i}) \varepsilon_\mathbf{i}. \tag{10}$$

A well-known sufficient condition for the global asymptotic stability of this system is that the matrix $\mathbf{A}(\mathbf{s_i})$ is positive definite. Unfortunately, due to the complex analytical form of $\mathbf{A}(\mathbf{s_i})$, we were not able of formally proving its positiveness. Nevertheless, the existence, uniqueness and local stability of the equilibrium point can be obtained thanks to the following property, which is proven in the Appendix:

P1: *Property of* $\mathbf{A}(\mathbf{s_i}) = \mathbf{J_{si}} \widehat{\mathbf{J}_{\mathbf{si}}^{-1}}$

1) *The matrix* $\mathbf{A}(\mathbf{s_i})$ *has a non-zero determinant.*
2) *The eigenvalues of the matrix* $\mathbf{A}(\mathbf{s_i})$ *are all strictly positives.*

1) Equilibrium point: The existence of an equilibrium point is obvious as $\varepsilon_{\mathbf{i}} = \mathbf{0_{4\times 1}}$ leads to $\dot{\varepsilon}_{\mathbf{i}} = \mathbf{0_{4\times 1}}$. Using the first item of the property P1, it is also obvious that this equilibrium point is unique.

2) Local Stability: A system is said locally stable if its linearized form around the equilibrium point is asymptotically stable. Linearizing (10) around its equilibrium point $\varepsilon_{\mathbf{i}} = \mathbf{0_{4\times 1}}$, *i.e.* around $\mathbf{s_i} = \mathbf{s_{id}}$, one gets:

$$\dot{\varepsilon}_{\mathbf{i}} = -\lambda \mathbf{A}(\mathbf{s_{id}})\varepsilon_{\mathbf{i}} \tag{11}$$

A necessary and sufficient condition for asymptotic stability of this linear system is that the eigenvalues of the matrix $\mathbf{A}(\mathbf{s_{id}})$ are all positive. This is verified for any value of $\mathbf{s_{id}}$ according to the second item of the property P1.
Thus, the system (10) is locally asymptotically stable around its unique equilibrium point. Remarkably, this property holds for any actual value of (α, β), it was assumed in the control law, for simplification purposes, that $\alpha = \pi$ and $\beta = 0$.

C. Simulation study

In order to compare the two proposed parameterizations, as well as evaluating the practical robustness of the approaches, an extensive simulation study has been performed. Its main results are summarized in the next.
The first simulation result shows a major limitation of using $\mathbf{s}_1$ for visually servoing the instrument, in the particular case when the desired displacement involves a large reorientation around the instrument axis. In this example, the instrument is chosen to be perpendicular to the ultrasound plane, while the desired position is obtained from the initial one by a rotation of 180 deg. around the axis $(\bar{M}, \mathbf{k}_P)$. In the image, this means that points M_1 and M_2 have to be switched. Moreover, since in this example $\alpha = \pi$ and $\beta = 0$, both the simplified control laws ensure a perfect decoupling.
With the first set of parameters, $\mathbf{s}_1$, the trajectories of the two points are explicitly controlled. Thus, thanks to a proper decoupling, the points follow straight lines during transitions from initial to final positions. Therefore, for this particular task, the points merge at the image center, Fig. 4(a). At this stage, only one point can be measured and the visual servoing controller fails. This strictly reproduces a well-known problem of 2D point-based visual servoing for a conventional camera system, when a 180 deg. rotation is to be performed around the optical axis of a camera [17].

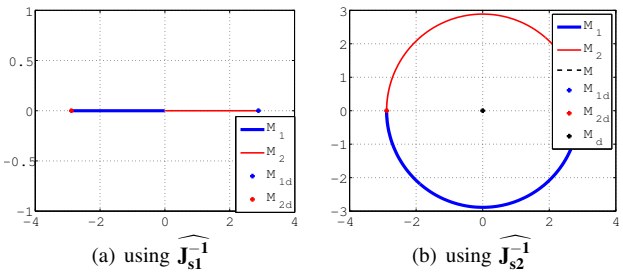

(a) using $\widehat{\mathbf{J}_{\mathbf{s1}}^{-1}}$ (b) using $\widehat{\mathbf{J}_{\mathbf{s2}}^{-1}}$

Fig. 4. Simulation results of a reorientation task: position in the image (mm)

Interestingly, when the same canonical example is fed to a controller based on the second parameterization $\mathbf{s}_2$, the results are much more satisfactory, see Fig. 4(b). The orientation of the instrument in the image is explicitly controlled while the system is decoupled. Thus the instrument is rotated around its own axis keeping both $\bar{M}$ and δ constant, and the desired position is reached without any visibility problems.
This canonical example illustrates the fact that explicitly controlling the image distance δ and the image angle θ provides strong superiority regarding the trajectories of the system in the image. For this reason, $\mathbf{s}_2$ was preferred to $\mathbf{s}_1$.
The proposed controller ensures a perfect decoupling in the particular case where the instrument is perpendicular to the US plane. However, in general, for $(\alpha, \beta) \neq (\pi, 0)$, only approximate decoupling is achieved. Therefore, errors on the components of $\mathbf{s}_2$ can become large. This may lead to a visibility problem as illustrated in Fig. 5(a). In this example, the system starts at a configuration where $\alpha = 110$ deg. and $\beta = 20$ deg. It can be seen in Fig. 5(a) that a strong error in δ occurs which leads to $\delta = 0$. At this time, the system is, again, not controllable as $M_1 \equiv M_2$.

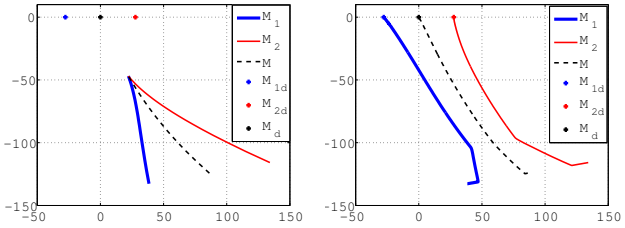

(a) using $\widehat{\mathbf{J}_{\mathbf{s2}}^{-1}}$ (b) using adaptive gains

Fig. 5. Simulation results of a large displacement task: position in the image (mm)

To cope with this problem, a gain adaptation mechanism is added to the controller. It is aimed at guaranteeing that the error on δ remains bounded, that is:

$$-\varepsilon_{\delta max} < \varepsilon_\delta < \varepsilon_{\delta max} \tag{12}$$

In other words, we want that:

- if $\varepsilon_\delta \geq \varepsilon_{\delta max}$ then $\dot{\varepsilon}_\delta < 0$
- if $\varepsilon_\delta \leq -\varepsilon_{\delta max}$ then $\dot{\varepsilon}_\delta > 0$

A simple control law that provides this property is:

$$\mathbf{u}' = \left[0,\ -\lambda \widehat{\mathbf{J}_{2,22}^{-1}} \varepsilon_\delta,\ 0,\ 0\right]^T \tag{13}$$

Indeed, the closed loop behavior for ε_δ is then:

$$\dot{\varepsilon}_\delta = -\lambda \mathbf{J}_{\delta,2} \widehat{\mathbf{J}_{2,22}^{-1}} \varepsilon_\delta \tag{14}$$

and $\mathbf{J}_{\delta,2}$ and $\widehat{\mathbf{J}_{2,22}^{-1}}$ have the same sign. However, obviously, the control law (13) does not allow for the three other coordinates of $\mathbf{s}_2$ to converge. Therefore, the idea is to switch from $\mathbf{u}$ in (9) to $\mathbf{u}'$ in (13) when the error ε_δ reaches its bound. In order to avoid for chattering induced by switches between control laws, a continuous controller is implemented, which final form is:

$$\mathbf{u} = \rho \mathbf{u} + (1-\rho)\mathbf{u}' \tag{15}$$

where:

$$\rho = \begin{cases} 1 & \text{if } |\varepsilon_\delta| < \varepsilon_0 \\ \dfrac{\varepsilon_{\delta max} - |\varepsilon_\delta|}{\varepsilon_{\delta max} - \varepsilon_0} & \text{if } \varepsilon_0 \leq |\varepsilon_\delta| \leq \varepsilon_{\delta max} \\ 0 & \text{otherwise} \end{cases} \quad (16)$$

This control law corresponds to controller (9) if $|\varepsilon_\delta| < \varepsilon_0$, controller (13) if $|\varepsilon_\delta| > \varepsilon_{\delta max}$, and a linear interpolation between the two controllers when $\varepsilon_0 \leq |\varepsilon_\delta| \leq \varepsilon_{\delta max}$.
The previous simulation was finally repeated with this new adaptive mechanism. Figure 5(b) illustrates the efficiency of the approach. Indeed, it can be seen that the distance δ is well controlled, which leads to a correct instrument visibility along the path.

IV. Experimental results

A. Velocity control of a 6 DOF robot through a trocar

The robot used for the experiments is a Stäubli TX40 manipulator which has 6 DOF.
A problem arises from the fact that a 6 DOF velocity has to be sent to the robot while the visual servoing loop only provides a 4 DOF command, corresponding to the degrees of freedom left free by the fulcrum point constraint. This problem of manipulating through a trocar with a dexterous robot has already been considered in the literature. For example, in [18] a complex inverse geometrical procedure is proposed, which strongly relies on the robot kinematics. In the next, we propose an alternative solution, which does not depend on the robot kinematics. The velocity of the instrument expressed at the center of the trocar T, is:

$$\mathbf{v_I} = \begin{bmatrix} \mathbf{u^T} & \mathbf{u_T^T} \end{bmatrix}^\mathbf{T} \quad (17)$$

where $\mathbf{u_T} = \begin{bmatrix} v_x & v_y \end{bmatrix}^\mathbf{T}$ groups the components of the velocity at point T perpendicular to the instrument axis. Thus the velocity expressed at the end effector of the robot is[2]:

$$\underbrace{\begin{bmatrix} {}^0\Omega(\mathbf{O_6}/\mathbf{0}) \\ {}^0\mathbf{V}(\mathbf{O_6}/\mathbf{0}) \end{bmatrix}}_{\mathbf{v_R}} = \underbrace{\begin{bmatrix} \mathbf{R_{0\to I}} & \mathbf{0_{3x3}} \\ \left[{}^0\mathbf{d}_{\mathbf{O_0O_6}}\right]_\times \mathbf{R_{0\to I}} & \mathbf{R_{0\to I}} \end{bmatrix} \begin{bmatrix} 0 & 0 & 1 & 0 & 0 & 0 \\ 1 & 0 & 0 & 0 & 0 & 0 \\ 0 & 0 & 0 & 1 & 0 & 0 \\ 0 & 0 & 0 & 0 & 1 & 0 \\ 0 & 0 & 0 & 0 & 0 & 1 \\ 0 & 1 & 0 & 0 & 0 & 0 \end{bmatrix}}_{:=\mathbf{F}} \mathbf{v_I} \quad (18)$$

This velocity is transformed into a desired joint position for the robot controller by the use of the robot inverse jacobian and a numerical integration, Fig. 6.

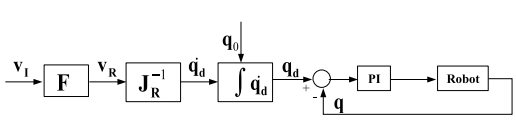

Fig. 6. Robot control law

While the 4 DOF of the instrument in $\mathbf{u_I}$ are controlled by the visual servoing loop, the two remaining velocities can be set to $\mathbf{u_T} = \begin{bmatrix} 0 & 0 \end{bmatrix}^\mathbf{T}$ in order to provide a null velocity at the fulcrum point. However, this corresponds to an open loop integration and leads to a drift of the fulcrum point T. To solve this problem, the idea is to calculate a desired velocity $\mathbf{u_T}$ from the error position between the instrument shaft axis and the fixed trocar center T. The trocar center position T is known during a surgical procedure as it can be recorded when inserting the instrument at the beginning of the operation. Therefore, from the robot geometrical model, it is always possible to compute the vector $\boldsymbol{\varepsilon_T}$ from the instrument shaft to point T, perpendicularly to the instrument shaft axis, see Fig. 7(a).

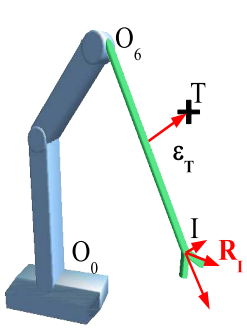

(a) Geometrical description

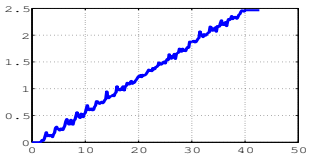

(b) Open-loop (mm vs s)

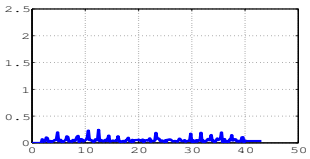

(c) Closed-loop (mm vs s)

Fig. 7. Distance between the instrument shaft and the fixed trocar fulcrum point

From this error, the proposed control law for $\mathbf{u}_T$ is:

$$\mathbf{u_T} = \lambda \mathbf{I_{2x2}}\ \boldsymbol{\varepsilon_T} \quad (19)$$

The complete control law is then:

$$\mathbf{v_I} = \begin{bmatrix} \mathbf{u} \\ \mathbf{u_T} \end{bmatrix} = \lambda \begin{bmatrix} \widehat{\mathbf{J}_{s2}^{-1}} & \mathbf{0_{2x2}} \\ \mathbf{0_{2x2}} & \mathbf{I_{2x2}} \end{bmatrix} \begin{bmatrix} \boldsymbol{\varepsilon_2} \\ \boldsymbol{\varepsilon_T} \end{bmatrix} \quad (20)$$

Noticing that $\dot{\boldsymbol{\varepsilon}}_\mathbf{T} = -\mathbf{u_T}$, the closed loop behavior becomes:

$$\begin{bmatrix} \dot{\boldsymbol{\varepsilon}}_\mathbf{2} \\ \dot{\boldsymbol{\varepsilon}}_\mathbf{T} \end{bmatrix} = -\lambda \begin{bmatrix} \mathbf{A}(\mathbf{s_2}) & \mathbf{J}_{\text{coupling}} \\ \mathbf{0_{2x2}} & \mathbf{I_{2x2}} \end{bmatrix} \begin{bmatrix} \boldsymbol{\varepsilon_2} \\ \boldsymbol{\varepsilon_T} \end{bmatrix} \quad (21)$$

where $\mathbf{J}_{\text{coupling}}$ is a coupling matrix. The error $\boldsymbol{\varepsilon_T}$ is a time varying function decoupled from $\boldsymbol{\varepsilon_2}$ which exponentially converges toward zero. As a result, the drift on the instrument w.r.t the fulcrum point is canceled. This is experimentally evidenced in Fig. 7. In these experiments, the robot was instructed to make a displacement of the instrument of about 25 pixels in the image thanks to a rotation around T, back and forth, 20 times. Fig. 7 shows the distance between the instrument axis and point T in two cases: a)with an open loop controller for $\mathbf{u_T}$ and b)with the closed loop controller (19). The drift observed in Fig. 7(b) is clearly canceled in Fig. 7(c) as the positioning error constantly remains less than 0.25 mm. Notably, the local stability of the visual servoing loop is preserved. Indeed, the complete closed loop transfer matrix of the system, in Eq. (21) is block triangular. Therefore, the linearized model is also block triangular, *i.e.* local stability is obtained if and only if $\mathbf{A}(\mathbf{s_{d2}})$ and $\mathbf{I_{2x2}}$ are

[2]In this paper $\left[{}^\mathbf{C}\mathbf{a}\right]_\times$ denotes the skew symmetric matrix associated with ${}^\mathbf{C}\mathbf{a}$, so that for any vector ${}^\mathbf{C}\mathbf{b}$, $\left[{}^\mathbf{C}\mathbf{a}\right]_\times {}^\mathbf{C}\mathbf{b} = {}^\mathbf{C}\mathbf{a} \times {}^\mathbf{C}\mathbf{b}$.

both regular and with positive eigenvalues only, which is obvious from the stability analysis of the visual servoing loop.

B. In vivo experiment

In vivo experiments have been performed with a pig at the Surgical School of Paris –APHP, Fig. 8. In these experiments,

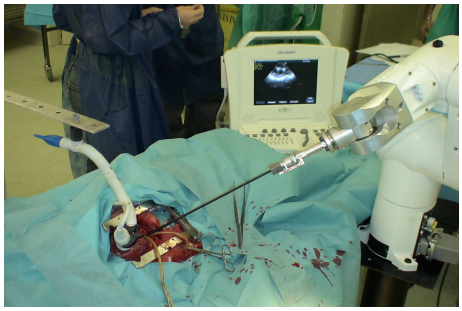

Fig. 8. In vivo set-up

the ultrasound probe is manually maintained in contact with the heart as transoesophagus probes cannot be used on pigs. The experiment is performed as follows:
The user specifies the desired goal in the ultrasound image. Then the current instrument coordinates in the image and the corresponding error are calculated and transmitted to the visual servoing loop. Thereafter, the command velocity of the instrument is computed according to (3) and sent to the robot controller. Fig. 9 shows the in vivo experimental results.

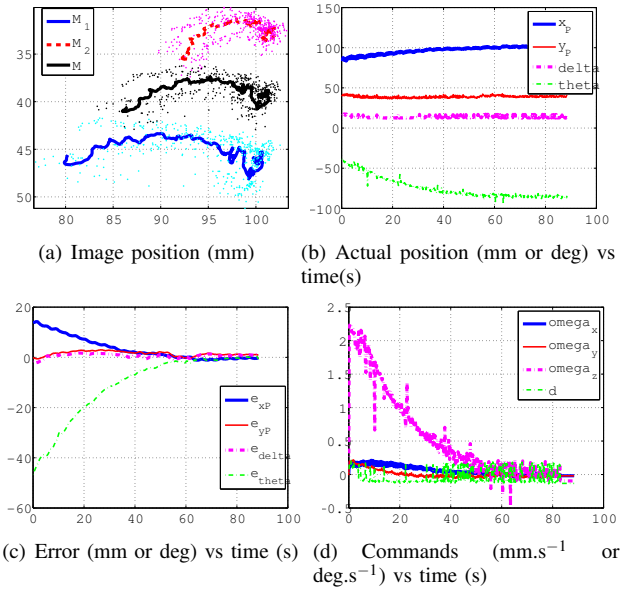

(a) Image position (mm)

(b) Actual position (mm or deg) vs time(s)

(c) Error (mm or deg) vs time (s)

(d) Commands (mm.s^{-1} or deg.s^{-1}) vs time (s)

Fig. 9. Results of in vivo experiment

These results are noisy because of motions of the instrument in the image resulting from the fact that the probe is in contact with the beating heart and thus moves. Eventhough, the error converges toward zero and the desired position is reached. Recall that during the whole experiment, it was never necessary to estimate where the probe was w.r.t. the robot, which emphasizes the simplicity and robustness of the approach.

V. Conclusion

A robotic system with ultrasound imaging has been presented. It uses ultrasound-based visual servoing to control the position of an instrument inside the heart.
Two possible controllers, equally robust with regards to their proven stability properties, were compared in simulation. This study exhibited behaviors that can directly be compared with conventional visual servoing based on projective cameras. Remarkably, the controller does not require any explicit model for the location of the probe with respect to the robot. In vivo experiments were successfully performed showing good robustness.
Future work may focus on eye-in-hand visual servoing from ultrasound by the use of a miniaturized probe.

Appendix

The Image Jacobian

In order to compute for $\dot{\mathbf{s}}_1$ with respect to $\mathbf{u}$, one first writes $\dot{\mathbf{s}}_1$ in the base $\mathscr{B}_M$:

$$\dot{\mathbf{s}}_1 = \underbrace{\begin{bmatrix} \cos\theta & 0 & -\sin\theta & 0 \\ 0 & \cos\theta & 0 & -\sin\theta \\ \sin\theta & 0 & \cos\theta & 0 \\ 0 & \sin\theta & 0 & \cos\theta \end{bmatrix}}_{=\mathbf{R}_1} \underbrace{\begin{bmatrix} {}^M\mathbf{V}(\mathbf{M_i}/\mathscr{P})_\mathbf{x} \\ {}^M\mathbf{V}(\mathbf{M_2}/\mathscr{P})_\mathbf{x} \\ {}^M\mathbf{V}(\mathbf{M_1}/\mathscr{P})_\mathbf{y} \\ {}^M\mathbf{V}(\mathbf{M_2}/\mathscr{P})_\mathbf{y} \end{bmatrix}}_{=\mathbf{v}_1}$$

Thus, the image jacobian $\mathbf{J}_{\mathbf{s}1}$ can be decomposed as:

$$\mathbf{J}_{\mathbf{s}1} = \mathbf{R}_1\mathbf{J}_1 = \mathbf{R}_1\begin{bmatrix}\mathbf{J}_{\mathbf{M_{1x}}} & \mathbf{J}_{\mathbf{M_{2x}}} & \mathbf{J}_{\mathbf{M_{1y}}} & \mathbf{J}_{\mathbf{M_{2y}}}\end{bmatrix}^T$$

where

$$\mathbf{J}_{\mathbf{M_{ix}}} = \begin{bmatrix} \frac{l_i + dt_z}{D} & \frac{t_{ix}}{D} & \frac{(l_i t_z + d)N\tan\alpha}{D} & \frac{l_i t_{ix} N\tan\alpha}{D} \end{bmatrix}$$
$$\mathbf{J}_{\mathbf{M_{iy}}} = \begin{bmatrix} 0 & 0 & \frac{l_i t_z + d}{\cos\alpha} & \frac{l_i t_{ix}}{\cos\alpha} \end{bmatrix}$$
$$N = t_{ix}\cos\beta + t_z\sin\beta \quad D = t_{ix}\sin\beta - t_z\cos\beta$$

In order to compute for $\dot{\mathbf{s}}_2$ with respect to $\mathbf{u}$, one first writes $\dot{\mathbf{s}}_2$ in the base $\mathscr{B}_M$:

$$\dot{\mathbf{s}}_2 = \underbrace{\begin{bmatrix} \cos\theta & 0 & -\sin\theta & 0 \\ 0 & 1 & 0 & 0 \\ \sin\theta & 0 & \cos\theta & 0 \\ 0 & 0 & 0 & 1 \end{bmatrix}}_{=\mathbf{R}_2} \underbrace{\begin{bmatrix} {}^M\mathbf{V}(\mathbf{P}/\mathscr{P})_\mathbf{x} \\ \dot{\delta} \\ {}^M\mathbf{V}(\mathbf{P}/\mathscr{P})_\mathbf{y} \\ \dot{\theta} \end{bmatrix}}_{=\mathbf{v}_2}$$

Thus, the image jacobian $\mathbf{J}_{\mathbf{s}2}$ can be decomposed as:

$$\mathbf{J}_{\mathbf{s}2} = \mathbf{R}_2\mathbf{J}_2 = \mathbf{R}_2\begin{bmatrix}\mathbf{J}_{\mathbf{Px}} & \mathbf{J}_\delta & \mathbf{J}_{\mathbf{Py}} & \mathbf{J}_\theta\end{bmatrix}^T$$

where:

$$\mathbf{J}_{\mathbf{Px}} = \frac{1}{2c_+c_-}\begin{bmatrix} (l_1 + d\cos\varphi)c_+ + (l_2 + d\cos\varphi)c_- \\ \sin\varphi(c_+ - c_-) \\ \tan\alpha((l_2 + d\cos\varphi)c_-s_+ - (l_1 + d\cos\varphi)c_+s_-) \\ \tan\alpha\sin\varphi(l_1s_-c_+ + l_2s_+c_-) \end{bmatrix}^T$$

$$\mathbf{J}_{\mathbf{Py}} = \frac{1}{2\cos\alpha}\begin{bmatrix} 0 \\ 0 \\ -(l_1+l_2)\cos\varphi + 2d \\ \sin\varphi(l_2 - l_1) \end{bmatrix}^T \quad \mathbf{J}_\theta = \frac{1}{\cos\alpha}\begin{bmatrix} 0 \\ 0 \\ \sin\beta \\ \cos\beta \end{bmatrix}^T$$

$$\mathbf{J}_\delta = \frac{1}{c_+ c_-}\begin{bmatrix} d\cos\varphi(c_- - c_+) \\ -\sin\varphi(c_+ + c_-) \\ \tan\alpha((l_2\cos\varphi + d)s_+ c_- + (l_1\cos\varphi + d)c_+ s_-) \\ \tan\alpha\sin\varphi(l_1 s_- c_+ - l_2 s_+ c_-) \end{bmatrix}^T$$

$$c_+ = \cos(\varphi+\beta)\ ,\ c_- = \cos(\varphi-\beta)$$
$$s_+ = \sin(\varphi+\beta)\ ,\ s_- = \sin(\varphi-\beta)$$

PROOF OF THE PROPERTY P1

Hereafter the matrix $\mathbf{B_i}$ will denote $\mathbf{B_i} = \mathbf{J_i}\,\widehat{\mathbf{J_i^{-1}}}$.

As $\mathbf{A(s_i)} = \mathbf{J_{si}}\,\widehat{\mathbf{J_{si}^{-1}}} = \mathbf{R_i B_i R_i^T}$, the matrices $\mathbf{A(s_i)}$ and $\mathbf{B_i}$ are similar. Thus, their eigenvalues are equal.

Furthermore, the matrix $\mathbf{B_i}$ is block triangular, it can be written as: $\mathbf{B_i} = \begin{bmatrix} \mathbf{C_i} & \mathbf{E_i} \\ \mathbf{0}_{2\times 2} & \mathbf{D_i} \end{bmatrix}$. The eigenvalues of the matrix $\mathbf{B_i}$ are then positive if and only if the eigenvalues of the two submatrices $\mathbf{C_i}$ and $\mathbf{D_i}$ are positive.

As $\mathbf{C_i}$ is a matrix $(2,2)$, its eigenvalues are positive if tr $\mathbf{C_i} > 0$ and det $\mathbf{C_i} > 0$.

The same condition can be written for the matrix $\mathbf{D_i}$.

If these conditions are verified, the eigenvalues of the matrix $\mathbf{A(s_i)}$ are all strictly positive.

Furthermore, the determinant of the matrix $\mathbf{A(s_i)}$ writes $\det\mathbf{A(s_i)} = \det\mathbf{R_i}\det\mathbf{B_i}\det\mathbf{R_i^T}$. It is obvious that $\det\mathbf{R_i} = \det\mathbf{R_i^T} = 1$. Thus $\det\mathbf{A(s_i)} = \det\mathbf{B_i}$.

The matrix $\mathbf{B_i}$ is bloc triangular, its determinant is $\det\mathbf{B_i} = \det\mathbf{C_i}\det\mathbf{D_i}$.

If the eigenvalues of the matrices $\mathbf{C_i}$ and $\mathbf{D_i}$ are positive, then $\det\mathbf{A(s_i)} = \det\mathbf{B_i} \neq 0$.

One can write:

$$\mathbf{C_1} = \frac{\cos\varphi}{\widehat{\Delta_2}}\begin{bmatrix} \dfrac{2d\cos\varphi + l_1 + l}{c_-} & \dfrac{l_1 - l}{c_-} \\ \dfrac{l_2 - l}{c_+} & \dfrac{2d\cos\varphi + l_2 + l}{c_+} \end{bmatrix}$$

$$\mathbf{D_1} = \frac{d}{\cos\alpha\widehat{\Delta_1}}\begin{bmatrix} l_1 + l - 2l_1 l\cos\varphi & l - l_1 \\ l - l_2 & l_2 + l - 2l_2 l\cos\varphi \end{bmatrix}$$

with $\widehat{\Delta_1} = 2l(l\cos\varphi + d)$ and $\widehat{\Delta_2} = 2(d\cos\varphi + l)$;

$$\mathbf{C_2} = \frac{\cos\varphi}{c_+ c_-}\begin{bmatrix} \dfrac{(l_1 + d\cos\varphi)c_+ + (l_2 + d\cos\varphi)c_-}{2(d\cos\varphi + l)} & \dfrac{\sin\beta\sin\varphi}{2} \\ -\dfrac{2d\cos^2\varphi\sin\varphi\sin\beta}{d\cos\varphi + l} & \dfrac{c_+ + c_-}{2} \end{bmatrix}$$

$$\mathbf{D_2} = \frac{1}{\cos\alpha}\begin{bmatrix} -\dfrac{(l_1 + l_2)\cos\varphi + 2d}{2(d + l\cos\varphi)} & -\dfrac{\sin\varphi(l_2 - l_1)}{2} \\ -\dfrac{\sin\beta}{d + l\cos\varphi} & -\cos\beta \end{bmatrix}$$

One can easily verify that trace and determinant are positive for each of the four matrices $\mathbf{C_1}$, $\mathbf{D_1}$, $\mathbf{C_2}$ and $\mathbf{D_2}$. Thus the matrices $\mathbf{A(s_1)}$ and $\mathbf{A(s_2)}$ have all theirs eigenvalues strictly positives and a non zero determinant.

The properties of the matrix $\mathbf{A(s_i)}$ are proven.

ACKNOWLEDGMENTS

The financial support of the CNRS P.I.R. Robea program (project GABIE) is gratefully acknowledged. Thanks to the partners of this project: LIRMM, Montpellier, TIMC, Grenoble, CEA-LIST, CHUG, Grenoble.

REFERENCES

[1] L. Angelini and M. Caratozzolo. Intraoperative echography: the state of the art. *Ann. Ital. Chir*, 70(2):223–230, 1999.

[2] D. de Cunha, P. Gravez, C. Leroy, E. Maillard, J. Jouan, P. Varley, M. Jones, M. Halliwell, D. Hawkes, P.N.T. Wells, and L. Angelini. The midstep system for ultrasound guided remote telesurgery. In *IEEE Engineering in MEdicine and Biology Society*, volume 20, pages 1266–1269, 1998.

[3] A. Vilchis, J. Troccaz, P. Cinquin, A. Guerraz, F. Pellisier, P. Thorel, B. Tondu, F. Courrges, G. Poisson, M. Althuser, and J. Ayoubi. Experiments with the ter tele-echography robot. In *Medical Image Computing and Computer-Assisted Intervention - MICCAI 2002: 5th International Conference, Proceedings, Part I*, pages 138 – 146, Tokyo, Japan, 2002.

[4] C. Delgorge, F. Courrges, L. Al Bassit, C. Novales, C. Rosenberger, N. Smith-Guerin, C. Brù, R. Gilabert, M. Vannoni, G. Poisson, and P. Vieyres. A tele-operated mobile ultrasound scanner using a light-weight robot. In *IEEE Trans. on information technology in biomedicine*, pages 50–58, 2005.

[5] A. Gourdon, P. Poignet, G. Poisson, Y. Parmantier, and P. Marche. Master slave robotic system for ultrasound scanning. In *IEEE Medical and Biological Engineering Conference, Proceedings*, Vienna, Austria, 1999.

[6] E.M. Boctor, G. Fischer, M.A. Choti, G. Fichtinger, and R.H. Taylor. A dual-armed robotic system for intraoperative ultrasound guided hepatic ablative therapy : A prospective study. In *IEEE ICRA International Conference on Robotique and Automation*, pages 2517–2522, New Orleans, LA, 2004.

[7] L. Phee, D. Xiao, J. Yuen, C. Fatt Chan, H. Ho, C. Hua Thng, C. Cheng, and W. Sing Ng. Ultrasound guided robotic system for transperinal biopsy of the prostate. In *Proc. of the ICRA 2005*, pages 1315–1320, 2005.

[8] J. Stoll, P. Dupont, and R. Howe. Ultrasound-based servoing of manipulators for telesurgery. In *Telemanipulator and Telepresence Technologies VIII Conference*, volume 4570 of *Proceedings of SPIE*, 2001.

[9] G. Megali, O. Tonet, C. Stefanini, M. Boccadoro, V. Papaspyropoulos, L. Angelini, and P. Dario. A computer-assisted robotic ultrasound-guided biopsy system for video-assisted surgery. In *Medical Image Computing and Computer-Assisted Intervention - MICCAI 2001: 4th International Conference, Proceedings*, pages 343–350, Utrecht, The Netherlands, 2001.

[10] S.E. Salcudean, W.H. Zhu, P. Abolmaesumi, S. Bachmann, and P.D. Lawrence. A robot system for medical ultrasound. *Robotics Research*, May 2000.

[11] A. Krupa. Automatic calibration of a robotized 3d ultrasound imaging system by visual servoing. In *IEEE Int. Conf. on Robotics and Automation, ICRA'2006*, pages 4136–4141, Orlando, Florida, May 2006.

[12] J. Hong, T. Dohi, M. Hashizume, K. Konishi, and N. Hata. An ultrasound-driven needle insertion robot for percutaneous cholecystostomy. *Physics in Medicine and Biology*, 49(3):441–455, 2004.

[13] M.-A. Vitrani, G. Morel, and T. Ortmaier. Automatic guidance of a surgical instrument with ulatrasound based visual servoing. In *Proc. of the ICRA 2005*, Barcelona - Spain, April 2005.

[14] M.-A. Vitrani, G. Morel, N. Bonnet, and M. Karouia. A robust ultrasound-based visual servoing approach for automatic guidance of a surgical instrument with in vivo experiments. In *BIOROB'06, IEEE Int. Conf. on Biomedical Robotics and Biomechatronics*, Pisa, Italy, February 2006.

[15] T. Ortmaier, M.-A. Vitrani, G. Morel, and S. Pinault. Robust real-time instrument tracking in ultrasound images. In *Proc. of SPIE Medical Imaging Conference*, San Diego, California, USA, February 2005.

[16] E. Malis and F. Chaumette. Theoretical improvements in the stability analysis of a new class of model-free visual servoing methods. *IEEE Transaction on Robotics and Automation*, 18(2):176–186, April 2002.

[17] F. Chaumette. Asservissement visuel. In W. Khalil, editor, *La commande des robots manipulateurs*, Trait IC2, chapter 3, pages 105–150. Herms, 2002.

[18] M. Michelin, E. Dombre, and P. Poignet. Geometrical control approaches for minimally invasive surgery. In *Medical Robotics, Navigation and Visualization (MRNV'04)*, pages 152–159, Remagen, Allemagne, 2004.